J. Fluid Mech. (1964), *vol.* 20, *part* 4, *pp.* 529–554
Printed in Great Britain

Long waves on the continental shelf: an experiment to separate trapped and leaky modes

By WALTER MUNK, FRANK SNODGRASS AND FREEMAN GILBERT

Institute of Geophysics and Planetary Physics, University of California, La Jolla

(Received 11 May 1964)

Random fluctuations in sea level, ζ, in the frequency range 0·1–60 cycles per hour were measured along the coast near Oceanside, California, where the coastline and bottom contours are fairly straight and parallel for 30 km. The two-dimensional covariance

$$R(\eta,\tau) = \langle \zeta(y,t)\,\zeta(y+\eta,t+\tau)\rangle$$

was computed for points separated by various distances η along the coast. The Fourier transform

$$S(f,n) = \iint R(\eta,\tau)\exp\left[2\pi i(n\eta+f\tau)\right]d\eta\,d\tau$$

gives the contribution towards the 'energy' $\langle\zeta^2\rangle$ per unit temporal frequency f per unit spacial frequency (long-shore component) n. It is found that most of the energy is confined to a few narrow bands in (f,n) space, and these observed bands correspond very closely to the gravest trapped modes (or edge waves) computed for the actual depth profile. The bands are 0·02 cycles per km wide, which equals the theoretical resolution of the 30 km array. Very roughly $S(f,n) \approx S(f,-n)$, corresponding to equal partition of energy between waves travelling up and down the coast. Theory predicts 'Coriolis splitting' between the lines $f^{\pm}(n)$ corresponding to these oppositely travelling waves, but this effect is below the limit of detection. The principal conclusion is that most of the low-frequency wave energy is trapped.

1. Introduction

The spectrum of ocean waves has a deep trough in the frequency range 0·1–60 cycles per hour (c/h) lying between the ocean tides and swell. Except for the occasional occurrence of 'tsunamis' (or 'tidal waves') these low-frequency low-energy waves typically have R.M.S.-amplitudes of 1 cm. as compared to 10^2 cm for tides or swell. Typical lengths of these 1 cm waves are from 5 to 100 km, and our interest derives from the fact that these dimensions are characteristic of the width of the continental shelf. Accordingly, we should expect (i) constructive interference between incident and reflected waves of appropriate dimensions, and (ii) the trapping of energy into a continental wave-guide, corresponding to the well-known leaky modes and trapped modes of wave-guide theory; in the former case energy is re-radiated into the deep sea, whereas in the latter case it remains trapped indefinitely under idealized conditions.

The first mathematical treatment of trapped waves over an inclined bottom goes back to Stokes, who considered his solution a curiosity (Lamb 1932, p. 447). Ursell (1952) generalized the solution to an infinite set of discrete modes, including the Stokes 'edge waves' as the fundamental mode. Ultimately all these solutions decay monotonically in a seaward direction, so that the energy remains trapped near shore; hence the name 'edge waves'.

The first observational evidence for the existence of edge waves occurred in August 1954. The hurricane CAROL formed near the Bahamas and then moved northward along the American East Coast at something like 17 m sec^{-1}. Redfield & Miller (unpublished manuscript) noted that the passage of the hurricane was followed by a series of 'resurgences' in sea level with a period of 5·5 h and a height of 1 m. Munk, Snodgrass & Carrier (1956) suggested that the resurgences were in fact a wake of edge waves. Their argument is as follows: a wake behind a disturbance travelling at a speed U is characterized by a phase velocity $C = U$, and a period T (or wavelength λ) appropriate to this phase velocity. For Stokes edge waves over a bottom of slope β we then have

$$2\pi U = 2\pi C = g\beta T, \tag{1}$$

which yields $T = 5{\cdot}9$ h for $U = 17$ m sec^{-1}, $\beta = 5 \times 10^{-4}$, as compared to the observed period of 5·5 h. Further support for the edge wave hypothesis comes from Greenspan's (1956) calculations that the observed amplitudes are consistent with the dimensions of the travelling pressure spot. But these very long periods are not negligible as compared to the length of day, and Reid (1958) has shown

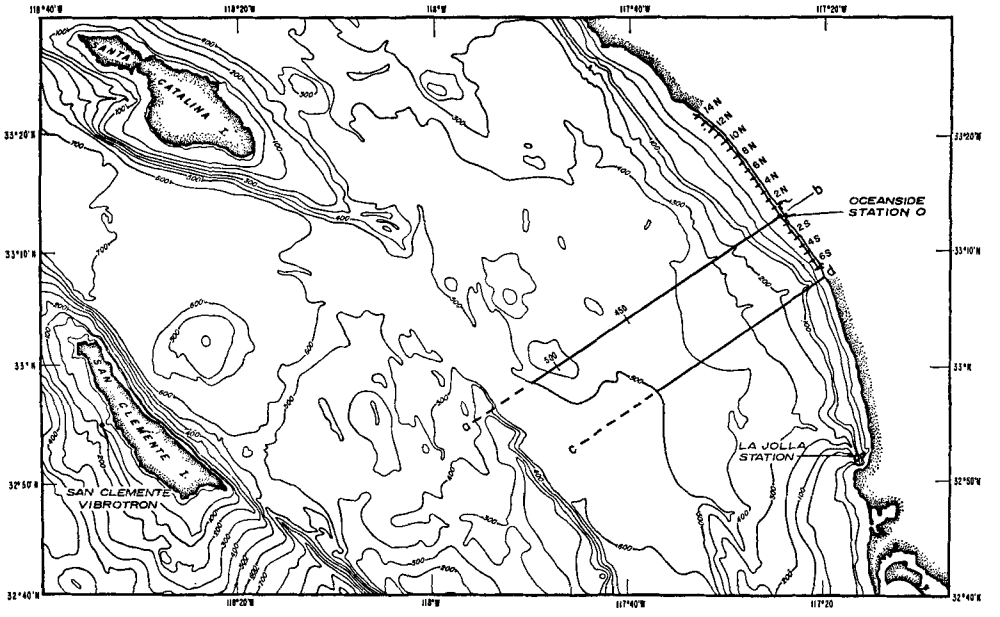

FIGURE 1. Topography off the coast of southern California (depth in fathoms). Location of instruments is indicated. Theoretical calculations were made for sections a–b and c–d, tending in the direction 236° T.

that the evidence somewhat deteriorates when the effect of Coriolis force is taken into account. Munk, Snodgrass & Carrier have also observed dispersive wave packets at Oceanside, California, following a sharp atmospheric gust at La Jolla (figure 1), the propagation of the packets being in accordance with the expected behaviour of edge waves. Donn & Ewing (1956) and Donn (1959) identified destructive waves along the Great Lakes with edge waves generated by travelling squall lines. We have generated edge waves in a wave tank, and found no difficulty in doing so even with crude equipment. (But we failed to generate observable edge waves by racing a destroyer at 31 knots along the 20-fathom line from La Jolla to Oceanside.)

So far the observational evidence refers to relatively clear-cut wave packets generated by impulsive or travelling sources of some simplicity. The question arises whether the complex wiggles which are always present on coastal tide records are associated with an 'edge-wave noise'. Power spectra of many low-frequency wave records (Munk, Snodgrass & Tucker 1959) revealed reproducible peaks at any given station associated with the width of shelf at this station. But it was not clear whether these were leaky or trapped waves, or in which direction they were travelling. To resolve these ambiguities, we performed a cross-spectral analysis between simultaneous low-frequency records at La Jolla and Oceanside (Munk *et al.* 1959, p. 360). The principle is as follows: let

$$\zeta(y,t) = a\cos 2\pi(ny - ft + \phi)$$

designate the departure in coastal water level associated with an elementary wave train at some distance y measured along shore. Assume stationarity in y and t, and random ϕ. The cross-correlation between records at a station at y and one at $y+\eta$ is then given by the time average

$$\begin{aligned} R(\eta,\tau) &= \langle \zeta(y,t)\,\zeta(y+\eta,t+\tau)\rangle \\ &= \tfrac{1}{2}a^2\cos 2\pi(n\eta - f\tau). \end{aligned} \tag{2}$$

We may now interpret $\frac{1}{2}a^2$ as the contribution $S(f)\,\delta f$ from all elementary wave trains in a narrow frequency band $f \pm \frac{1}{2}\delta f$ towards the variance:

$$\langle \zeta^2 \rangle = R(0,0) = \int S(f)\,df.$$

The expression

$$R(\eta,\tau) = \int S(f)\,[C_N(\eta,f)\cos 2\pi f\tau + Q_N(\eta,f)\sin 2\pi f\tau]\,df \tag{3}$$

defines the (normalized) co- and quadrature spectra. For the case of Stokes edge waves (equation (1)) comparison of (2) and (3) gives

$$C_N(\eta,f) + iQ_N(\eta,f) = \exp(i2\pi n\eta) = \exp[i(4\pi^2\eta/g\beta)f^2].$$

For a fixed separation η, the cross-spectrum oscillates with frequency as $\exp(if^2)$. Instead, we found that $C_N(\eta,f)$ vanishes after just one zero crossing, and $Q_N(\eta,f)$ is negligible throughout. At the time, the result appeared to contradict the edge-wave hypothesis. (We now know that Q_N is small because nearly equal energy is transmitted up and down the coast, and C_N is damped because of interference between multiple modes.) The experiment was repeated for the broad

Argentinian Shelf which is noted for its low-frequency waves, but all we really learned from the cross-spectral analysis was a clock error at one of the tide stations (Inman, Munk & Balay 1961).

So far then, the experiments had involved comparison of wave records at two coastal points. The complementary geometry involves two records separated along a line *normal* to shore. Here we could make good use of San Clemente Island about 100 km from the coast and almost half-way out on southern California's

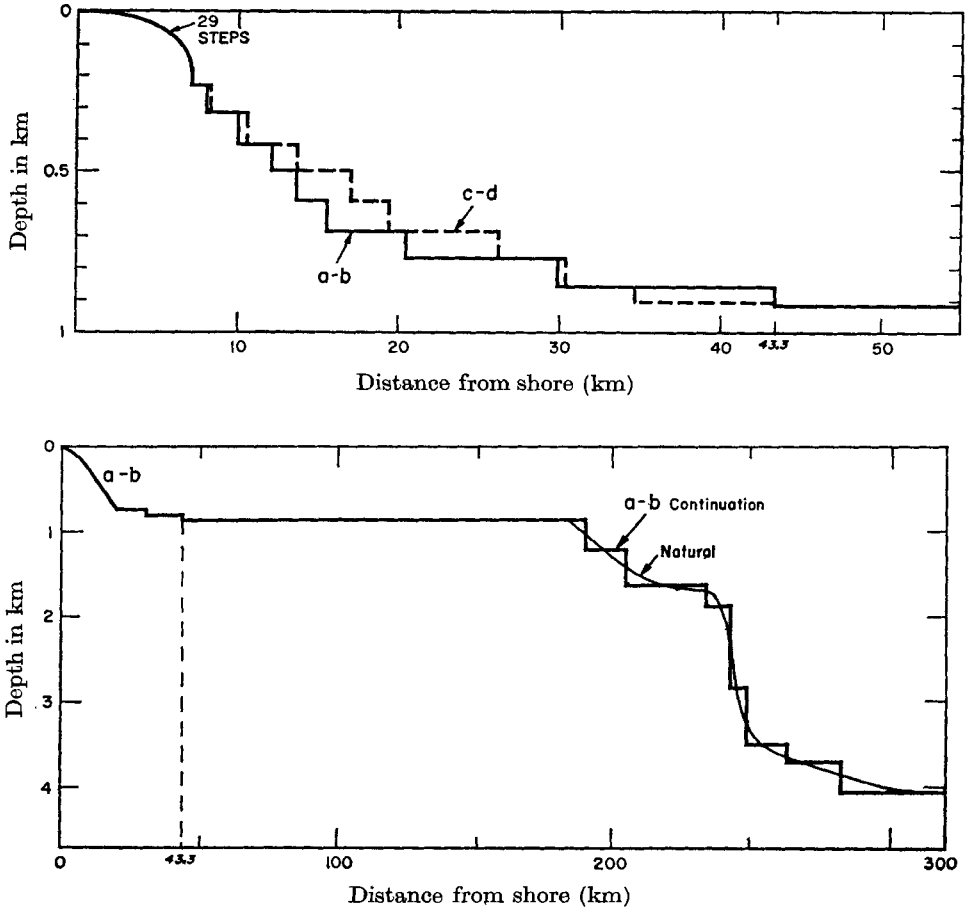

FIGURE 2. Profiles a–b and c–d (for location, see figure 1). The measured profile has been approximated by a series of steps (the first 29 are too small to be shown). The lower figure shows the continuation of a–b on a contracted scale, and the steps by which it has been approximated.

continental borderland (Snodgrass, Munk & Miller 1962). This is a hilly sea bottom averaging 0·6 km in depth and 250 km in width; beyond it the depth drops off sharply to 3·6 km. At the very low frequencies we found the two records highly coherent and in phase, as expected; there is a phase reversal at 0·7 c/h, thus indicating that above this frequency there is a nodal line between island and coast. A second reversal occurs near 1·7 c/h. Again, we found the quadrature

spectra to be small, and the co-spectra to decay rapidly with increasing frequency. Our interpretation was that comparable energies must be present in various modes.

We had then reached the conclusion that the wave energy is distributed in a most complicated way among the modes. A single station does not help, and even two stations are inadequate to decipher the situation. What is needed is a station *array*, yielding $R(\eta, \tau)$ over a range of values of the station separation η, from which the two-dimensional spectrum

$$S(n,f) = \iint R(\eta,\tau) \exp\left[2\pi i(n\eta + f\tau)\right] d\eta\, d\tau$$

can be computed without speculation and ambiguity. Here n is the long-shore component of the wave-number, measured in cycles per km (not radians per km), so that f and n are comparable units of temporal and spatial frequency. Accordingly, $S(n,f)$ is the energy per unit temporal frequency per unit spatial frequency, in units of

$$\rho g L^2(\text{cycle}/T)^{-1}\,(\text{cycle}/L)^{-1} = \rho g L^3 T;$$

the constant factor ρg is usually omitted. The integration

$$\int S(f,n)\, dn = S(f)$$

yields the one-dimensional power spectrum (units L^2T). This array experiment has now been performed with, as we shall show, quite definitive results; we wish we had done it sooner and not attempted the many experimental shortcuts.

2. Trapped and leaky modes

Figure 3 shows the computed (f, n) diagram for profiles a–b and c–d (figures 1 and 2). In the computation the smooth depth profiles are represented by a series of discontinuous steps. The equations are solved for each constant depth 'layer', and the solution patched by requiring continuity in the flux of mass and momentum across the steps. The procedure is best regarded as a scheme for numerically integrating the differential equations and it has been demonstrated (Volterra 1887) that the precise solution can be approached to any required precision by making the steps sufficiently small. Here the bottom profile is represented by 38 layers, starting with very narrow and shallow layers at the coast. The 38th layer is assumed to extend indefinitely at a depth of 915 m. In fact, the continental borderland does extend for almost 200 km at this average depth and waves shorter than 100 km can be adequately discussed ignoring what goes on beyond the shelf. But the drop beyond the shelf to the oceanic depths calls for certain re-interpretation of the (f, n) diagram (§9).

The linearized wave equation for constant depth is

$$\partial^2\zeta/\partial t^2 - c^2\nabla^2\zeta = 0.$$

Let x be drawn seaward, and y along the coastline pointing north. If there is no absorption in shallow water, then all waves (trapped or leaky) have a component travelling parallel to shore

$$\zeta = q(x) \exp 2\pi i(ny - ft),$$

and the wave profile normal to shore is determined by

$$d^2q/dx^2 - \beta^2 q = 0, \quad \beta^2 = 4\pi^2(f^2/c^2 - n^2),$$

with the solution

$$\left.\begin{aligned} q &= a\cos\beta x + b\sin\beta x && (\beta^2 > 0),\\ q &= a + bx && (\beta^2 = 0),\\ q &= a\cosh|\beta|x + b\sinh|\beta|x && (\beta^2 < 0). \end{aligned}\right\} \tag{4}$$

We are fully justified in making the shallow-water approximations; e.g. the water depth is everywhere small as compared to the wavelength. Then $c^2 = gh$, and the water motion is proportional to $\nabla\zeta$ and uniform from top to bottom.

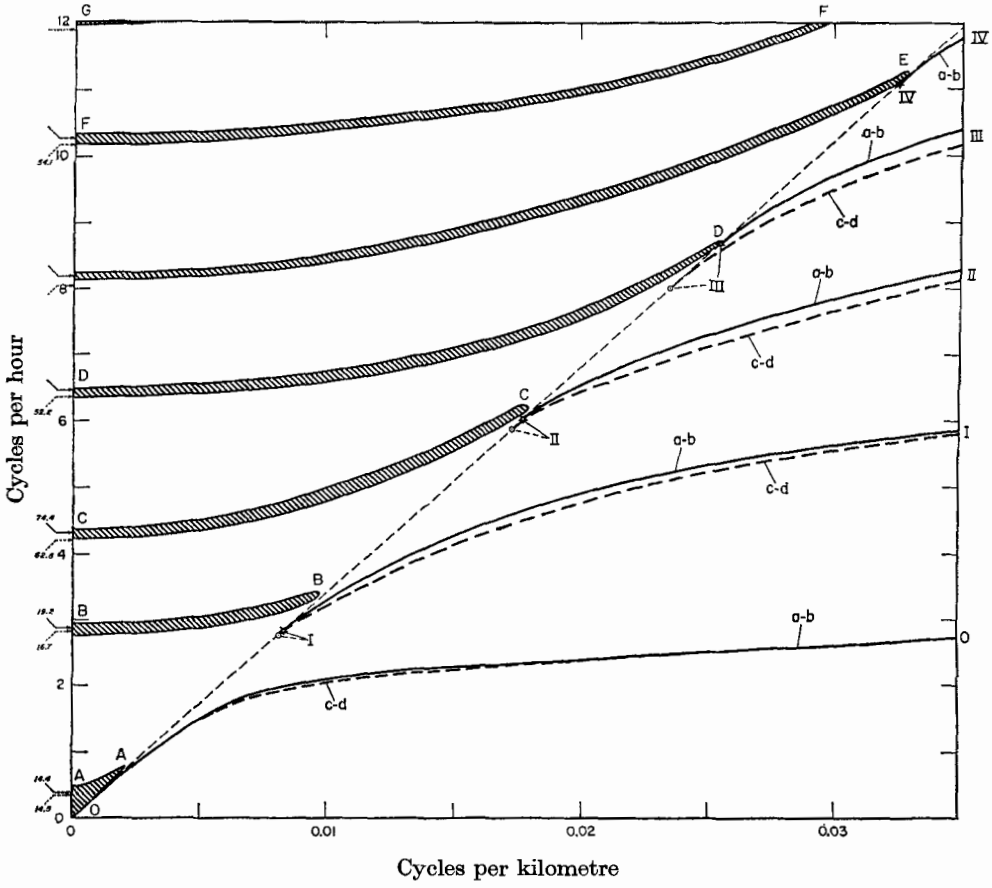

FIGURE 3. The computed (f, n) diagram for profiles a–b (solid curves) and c–d (dashed). The 45° line through the origin separates the trapped modes (right) from the leaky modes (left). The trapped modes (edge waves) emerge from the 45° line at the *cut-off frequencies*, which are labelled with the mode numbers 0, I, ..., IV in accordance with the number of nodes between the shore ($x = 0$) and $x = \infty$. The area between these *discrete* modes is forbidden. To the left is the *continuous* spectrum associated with incident waves of any given frequency and direction, varying from normal incidence ($n = 0$) to glancing incidence (the 45° line). The shaded bands (or leaky modes) A, B, ..., G include all combinations of f and n for which the coastal wave amplitude exceeds the incident amplitude. The bands are drawn for profile a–b only; arrows on the f-axis (solid for a–b, dashed for c–d) give frequencies and values of maximum amplification at normal incidence.

The boundary condition at the coastline ($x = 0$) is that the flow normal to shore must vanish, $q'(0) = 0$, with q' designating dq/dx. Let A be the amplitude at $x = 0$, and h_1 the depth of the first step. We may write

$$q_1(0) = A, \quad h_1 q_1'(0) = 0.$$

Let $q_2(0)$ and $q_2(\Delta_2)$ designate the amplitudes at the beginning ($x = \Delta_1$) and end ($x = \Delta_1 + \Delta_2$) of the second step. The patching conditions

$$q_2(0) = q_1(\Delta_1), \quad h_2 q_2'(0) = h_1 q_1'(\Delta_1)$$

assure continuity of water level and mass flux at $x = \Delta_1$, etc. The last two conditions are conveniently combined in the form

$$\mathbf{Q}_2(0) = \mathbf{Q}_1(\Delta_1), \tag{5}$$

where

$$\mathbf{Q}_i(x) = \begin{bmatrix} q_i(x) \\ h_i q_i'(x) \end{bmatrix}$$

is the designated column matrix.

Following Haskell (1953, 1960) it is now convenient to write the relations between $\mathbf{Q}_i$ at the beginning and end of each step in matrix form. According to equations (4), these relations are

$$\mathbf{Q}_i(\Delta_i) = \mathbf{B}\mathbf{Q}_i(0) \tag{6}$$

where

$$\mathbf{B}_i = \begin{bmatrix} \cos\beta_i\Delta_i & \sin\beta_i\Delta_i/\beta_i h_i \\ -\beta_i h_i \sin\beta_i\Delta_i & \cos\beta_i\Delta_i \end{bmatrix}$$

for $\beta_i^2 > 0$, and corresponding matrices for $\beta_i^2 = 0$ and $\beta_i^2 < 0$. It follows from (5) and (6) that

$$\mathbf{Q}_2(0) = \mathbf{Q}_1(\Delta_1) = \mathbf{B}_1\mathbf{Q}_1(0),$$
$$\mathbf{Q}_3(0) = \mathbf{Q}_2(\Delta_2) = \mathbf{B}_1\mathbf{B}_2\mathbf{Q}_1(0),$$

etc., so that for the last step

$$\mathbf{Q}_N(0) = \mathscr{C}\mathbf{Q}_1(0), \quad \mathscr{C} = \prod_{i=1}^{N-1} \mathbf{B}_i. \tag{7}$$

Take first the case of trapped waves. In order for the wave amplitude to remain finite over the last step we write

$$q_N = a\exp(-|\beta_N|x), \quad h_N q_N' = -|\beta_N| h_N a \exp(-|\beta_N|x)$$

and equation (7) becomes

$$\begin{bmatrix} a \\ -|\beta_N| h_N a \end{bmatrix} = \mathscr{C}\begin{bmatrix} A \\ 0 \end{bmatrix}. \tag{8}$$

This is a system of two equations in two unknowns, a and A. In order that a solution exist, the determinant

$$\mathscr{C}_{21} + |\beta_N| h_N \mathscr{C}_{11} \tag{9}$$

must vanish. For any given value of n, the values of f that cause the determinant to vanish are eigenvalues. Since n is a continuous parameter, the eigenvalues are curves $f(n)$. The determinant is real, and therefore has solutions only for $\beta_N^2 < 0$, e.g. $f < nc_N$. The line $f = nc_N$ in the (f, n) diagram where $\beta_N = 0$ is therefore the cut-off line.

For $f > nc_N$ the curve $f(n)$ does not simply vanish. In the complex f and n planes $\beta_N = 0$ is a branch point. The zero of equation (9) for a given mode goes

through the branch point at cut-off and on to the 'other' Riemann sheet of the complex f and n planes. As $n \to 0$ the zero approaches a value of f whose real part is precisely one of the organ pipe frequencies associated with the stack of layers when the last layer is 'rigid' ($q'_N(0) = 0$).

We shall not discuss this matter further but refer the reader to a paper by Rosenbaum (1960) for a detailed presentation.

Figure 3 was constructed on a digital computer. The procedure differs then according to whether β_N^2 is negative or positive, i.e. whether we are to the right or to the left of the '45° line' of slope c_n. In the former case the program evaluates $\mathscr{C}$ and the determinant (9) for trial values of f and converges upon the eigensolutions by an iterative scheme. The discrete modes emerge from the 45° line at certain cut-off frequencies which are the zeros of $\mathscr{C}_{21}$ in equation (9). In the latter case the program computes the ratio

$$r(f, n) = A/a$$

of coastal over incident amplitude. Shaded areas contain $r > 1$. Normal incidence ($n = 0$) is associated with certain resonances in the open organ pipe sense.

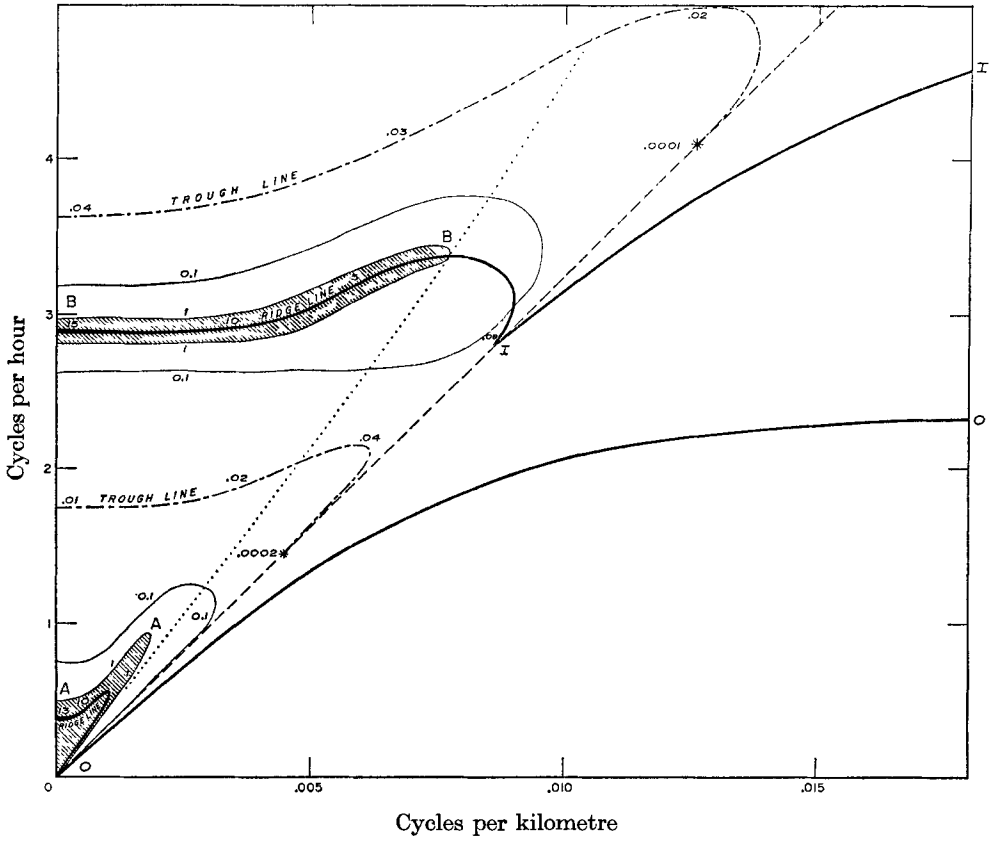

FIGURE 4. A somewhat schematic presentation of the connexions between leaky modes A, B, and trapped modes 0, I. Contours are for values 1 and 0·1 of the ratio, r, of costal to incident amplitude. Shaded bands designate $r > 1$. Ridges and trough lines are shown with selected values of r indicated.

Frequencies of peak amplification are indicated by the arrows along the f-axis of figure 3. The bands of amplification are narrow; thus the partial reflexions of the incident waves remove most of the energy before the wave reaches shore. The essential features are not changed as we deviate somewhat from normal incidence. But near glancing incidence the situation becomes complicated (figure 4). Here $r < 1$, i.e. the coastal amplitude is always less than the incident amplitude. Bands of amplification continue as ridges of minimum attenuation which curve sharply downward and terminate at the cut-off frequencies of the trapped modes. These features appear also in the simple two-step model (Snodgrass *et al.* 1962).

Certain features of the (f, n) diagram deserve consideration. The slope, df/dn, of the discrete modes is the group velocity, and the slope, f/n, of the chord is the phase velocity (both measured along shore). At the cut-off frequencies we find $df/dn = f/n = c_n = (gh_n)^{\frac{1}{2}}$; the waves are non-dispersive and travel at the velocity appropriate to the depth over the last step. At higher spatial frequencies the velocities diminish.

There are no corresponding relations $f(n)$ in the continuum, since all points of the (f, n) diagram to the left of the 45° line are legitimate solutions. Still one is tempted to regard the narrow amplification bands as broadened lines, and to speak of group and phase velocities by referring the slope and co-ordinates of these bands. For example, normal incidence is then associated with zero group velocity and infinite phase velocity. There is justification for this point of view. Suppose the incident radiation were suddenly to vanish. Then waves whose dimensions are appropriate to the amplification bands would remain prominent for some time, but gradually lose energy by radiation into the deep sea. We may regard these waves as leaky modes, with the line broadening resulting from the radiational losses.

3. Properties of a process $\zeta(y, t)$ which is stationary in both variables

The observational material $\zeta(y, t)$, needs to be presented in a form suitable for comparison with the theoretical (f, n) diagram. The transformations are first derived assuming complete symmetry in y and t. The relations appear then in the most compact and simple form. In actual fact the space and time co-ordinates are not quite interchangeable, and some of the symmetry needs to be sacrificed in the discussion of the observations.

We represent $\zeta(y, t)$ as a Fourier–Stieltjes integral

$$\zeta(y,t) = \int dH(n,f) \exp\left[2\pi i(ny + ft)\right] \tag{10}$$

where

$$dH(-n, -f) = dH^*(n,f) \tag{11}$$

in order for ζ to be real, and where

$$\langle dH(n_1,f_1)\, dH(n_2,f_2)\rangle = 0 \quad \text{if} \quad (n_1,f_1) \neq (n,f_2) \tag{12}$$

and

$$\langle dH(n,f)\, dH^*(n,f)\rangle = S(n,f)\, dn\, df. \tag{13}$$

The spectrum $S(n,f)$ is real and even, $S(n,f) = S(-n, -f)$. It follows from (10) to (13) that the spectrum is the Fourier transform of the covariance

$$\left.\begin{aligned} R(\eta,\tau) &= \langle \zeta(y,t)\,\zeta(y+\eta,t+\tau)\rangle, \\ S(n,f) &= \iint R(\eta,\tau)\exp\left[-2\pi i(n\eta+f\tau)\right]d\eta\,d\tau. \end{aligned}\right\} \tag{14}$$

We shall find it useful to introduce the mixed quantity

$$S'(\eta,f) = \int R(\eta,\tau)\exp\left(-2\pi i f\tau\right)d\tau \tag{15}$$

$$= \int S(n,f)\exp\left(2\pi i n\eta\right)dn. \tag{16}$$

Unlike $S(n,f)$, $S'(\eta,f)$ is a complex quantity, and we write

$$S'(\eta,f) = C'(\eta,f) + iQ'(\eta,f).$$

We refer to C' as the (unnormalized) displaced co-spectrum, to Q' as the displaced quadrature spectrum. Accordingly

$$\begin{aligned} C'(\eta,f) &= \tfrac{1}{2}[S'(\eta,f) + S'^{*}(\eta,f)] \\ &= \int S(n,f)\cos 2\pi n\eta\,dn \\ &= \int \tfrac{1}{2}[S(n,f) + S(-n,f)]\cos 2\pi n\eta\,dn, \end{aligned} \tag{17}$$

and similarly $$Q'(\eta,f) = \int \tfrac{1}{2}[S(n,f) - S(-n,f)]\sin 2\pi n\eta\,dn. \tag{18}$$

Hence $C'(\eta,f)$ depends only on the mean value of the energy density for waves travelling up or down the coast, whereas $Q'(\eta,f)$ depends on the difference.

It will be convenient to refer to the *normalized* cross-spectra

$$C'_N(\eta,f) = C'(\eta,f)/S'(0,f), \quad Q'_N(\eta,f) = Q'(\eta,f)/S'(0,f). \tag{19}$$

It follows from (16) and the fact that $S(n,f)$ is real that

$$S'(0,f) = C'(0,f) = \int S(\eta,f)\,dn = S(f)$$

is the conventional power spectrum. Dividing both sides of (17) and (18) by $S'(0,f)$ and inverting the Fourier transform, we obtain

$$\left.\begin{aligned} T^{+}(n,f) &= [S(n,f) + S(-n,f)]/S(f) = 2\int C'_N(\eta,f)\cos 2\pi n\eta\,d\eta, \\ T^{-}(n,f) &= [S(n,f) - S(-n,f)]/S(f) = 2\int Q'_N(\eta,f)\sin 2\pi n\eta\,d\eta. \end{aligned}\right\} \tag{20}$$

$T^{+}(n,f)\,\delta n$ is the fractional contribution to the power spectrum $S(f)$ from southward waves in the band $n \pm \frac{1}{2}\delta n$ plus that from northward waves in the band $-n \pm \frac{1}{2}\delta n$ (i.e. the fractional energy in $|n| \pm \frac{1}{2}\delta n$); $T^{-}(n,f)$ is the corresponding fractional difference, southward minus northward for positive n.

For the actual calculation the integrals are replaced by summations, and we are limited to frequencies below $1/2\Delta t$ and $1/2\Delta y$ by the sampling intervals Δt and Δy. In our experiment $\Delta t = 30$ sec and $\Delta y = 0{\cdot}73$ km and the corresponding limits are 60 c/h and 0·685 c/km. The limits are known as the Nyquist frequencies. Any contribution from higher frequencies is folded back and appears under the 'alias' of lower frequencies. The only safe procedure is to make sure that the spectra beyond the Nyquist frequencies are negligible as compared to the range of interest. After removal of sea and swell by the analogue filters this condition is satisfied.

4. Observations

Simultaneous measurements of sea bottom pressure were usually made at three stations. One instrument remained fixed off the boat basin north of Oceanside (station 0 on figure 1). The other two would occupy various positions north and south of station 0, extending as far as $14\frac{1}{2}$ Pet. miles† north and 7 Pet. miles south for maximum separation. The initial runs were as follows (all units in Pet. miles):

Run	South	Central	North	Separations
1	0	0	0	0, 0, 0 (calibration run)
2	0	$\frac{1}{2}$ N	$1\frac{1}{2}$ N	$\frac{1}{2}$, 1, $1\frac{1}{2}$
3	2 S	0	$2\frac{1}{2}$ N	2, $2\frac{1}{2}$, $4\frac{1}{2}$

The experiments were repeated until all *separations* 0, $\frac{1}{2}$, 1, ..., $21\frac{1}{2}$ Pet. miles (with some unavoidable overlaps) were achieved.

The instruments were installed 500 m from shore, at an average depth of 7 m. The location is the closest possible to shore beyond the surf zone.

Fluctuating wave pressures at each of the stations were measured by a Vibrotron pressure gauge (Snodgrass, Munk & Tucker 1958); in outline, the water pressure changes the tension of a taut wire and so changes its natural frequency. The wire is maintained in oscillation by a constant voltage supplied from shore, and the oscillation frequency is detected as a fluctuation in the electric current. In the present experiments it was necessary to attenuate the pressure changes due to the obvious short-period ocean waves, whose frequencies are typically 300 c/h and upwards. Each Vibrotron was therefore enclosed in a hydraulic filter that attenuated such short-period fluctuations by a factor of 10^5 or more; this filter has been described by Snodgrass (1964).

Each instrument was buried about 1 m deep into the sea bottom to protect it from temperature fluctuations. The time occupied by 10^5 oscillations of the Vibrotron (about 6 sec) was measured in microseconds and recorded digitally on punched paper tape. These measurements were made at intervals of 30 sec, and the observations extended over 50 h. Thus the data consisted of about 6000 numbers per instrument per run. The instruments were connected by underwater cable and the digital recording made at one site on shore.

† 1 Peterson mile = 4800 ft. = 1·46 km. The units were dictated by the length of cable on a standard spool. The associated unit of spatial frequency is 1 cycle per Peterson mile = 0·685 c/km. We are deeply indebted to Mr Frank Peterson for making the many underwater installations.

The routine data reduction was entirely performed by computer. This consisted of: (i) searching for data gaps and punching errors, and correcting these automatically whenever possible; (ii) removing tides by a digital high-pass filter; (iii) performing cross-spectral analyses for various frequency resolutions and ranges; (iv) correcting the spectra for instrument response; (v) plotting results and storing values on cards for subsequent spatial Fourier transforms. The reduction of the 18,000 observations taken on any one run was completed within a few hours of the end of the run, in time to make adjustments for the next run. This fulfils an old dream of carrying out data reduction almost in 'real time'.

The instrument sensitivity is roughly 0·003 cm of water pressure per least count, and the instrumental noise level is negligible as compared to the observed intensities. When the instruments were placed side by side, the coherence between the records was above 0·995 between 0 and 12 c/h.

5. Aperture synthesis

The two-dimensional spectra are the results of measurements taken at different times and in somewhat different locations. This presumes stationarity with respect to time and space. In radio astronomy, observations taken on successive nights with different antenna configurations are combined into a single 'radio photograph' of the sky, and this is referred to as 'aperture synthesis'. It is as if many snapshots with different lenses are combined into a single photograph. Here we may regard $S(n,f)$ a single photograph† of the radiation coming from various directions (determined by f/n) as synthesized from measurements over a year.

Figure 5 shows spectra $S(f)$, $C'_N(\eta,f)$, $Q'_N(\eta,f)$ on two successive runs.‡ The higher intensities during 5–6 May are probably associated with increased sea and swell activity (Hasselmann, Munk & MacDonald 1963), and, though some of the features are reproducible, there are substantial differences between the two spectra. In contrast, the normalized cross-spectra are reproduced in all essential detail. We interpret this result to mean that in any given frequency band the relative energy contribution from different modes is reasonably stationary, whereas the total energy in the band is not. All our plots refer to the normalized cross-spectra. The normalized quadrature spectrum is small compared to the co-spectrum, indicating approximately equal energy in northward and southward waves.

The situation is less satisfactory with respect to the space co-ordinate, y. When there is a large degree of overlap (figure 6) the results agree reasonably well. In the case of figure 7 the results for a 7 Pet. mile separation north of station 0 differ

† Our plot is one-dimensional, and over many different frequency bands. The radio photographs are two-dimensional but monochromatic, and they are concerned only with the *continuum*. The analogy is then far from complete, but the term 'aperture synthesis' applies well in both instances.

‡ $S(f)$ is taken as the geometric mean of the power spectra at the two stations separated by η. $S(f)$ is corrected for analogue filtering; the raw spectra drop off sharply at the Nyquist frequency (60 c/h). The normalized co- and quadrature spectra are independent of these corrections.

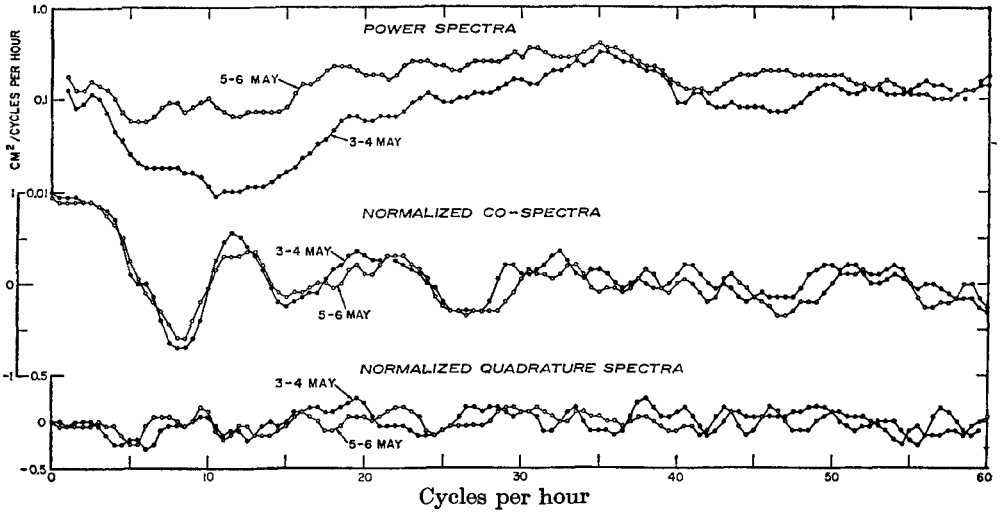

FIGURE 5. Comparative spectra $S(f)$, $C'_N(1\frac{1}{2}, f)$, $Q'_N(1\frac{1}{2}, f)$ on 3–4 and 5–6 May 1962 for stations 0 and $1\frac{1}{2}$ N.

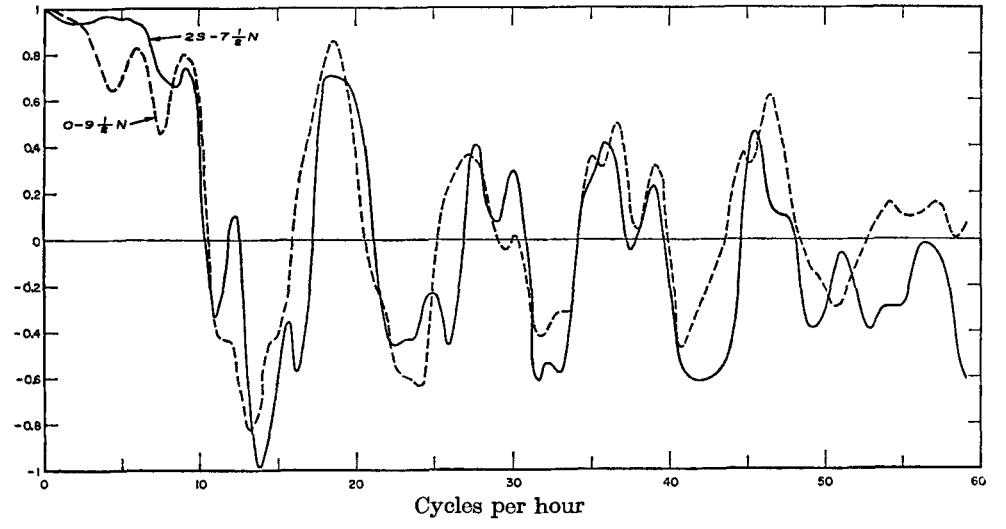

FIGURE 6. Displaced co-spectra $C'_N(9\frac{1}{2}, f)$ for stations 0–$9\frac{1}{2}$ N (22–25 March 1963) and 2S–$7\frac{1}{2}$ N (28 August to 8 September 1962).

substantially from those south of station 0. Undoubtedly this is associated with a narrowing of the shelf to the south (figure 1).

Figure 8 shows the normalized co-spectrum in (η, f) space for all measured values of η, from 0 to $21\frac{1}{2}$ Pet. miles at intervals of $\frac{1}{2}$ Pet. mile. The non-stationarity with respect to y is obvious. The separation $5\frac{1}{2}$ was achieved with two stations located further north than for adjoining separations, and there is a marked kink in the contours. Even more pronounced is the switch from northern to southern locations at $\eta = 15$ Pet. miles. To remove these kinks we have referred the field for $\eta \geqslant 15$ Pet. miles to some frequency scale f^* so chosen as to

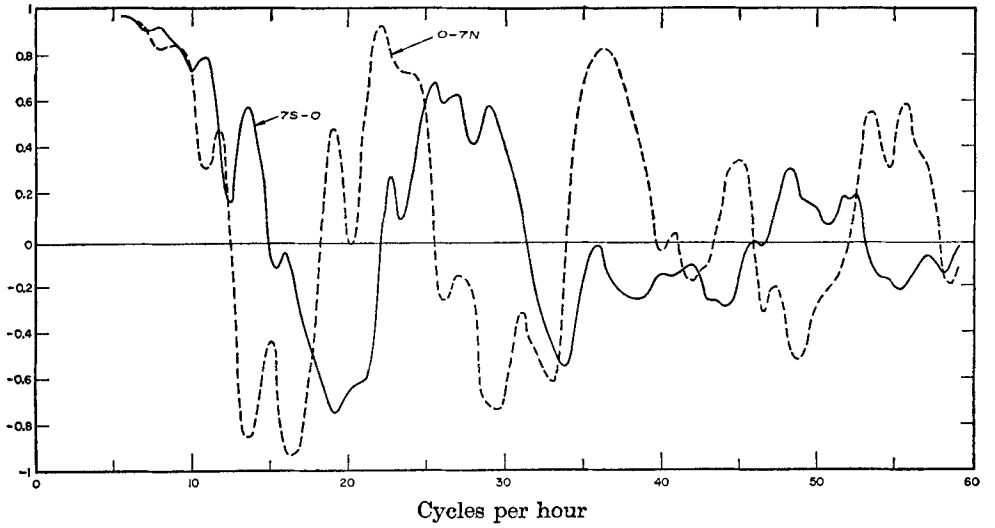

FIGURE 7. Displaced co-spectra $C'_N(7, f)$ for stations 0–7 N (8–10 April 1963) and 7 S–0 (11–14 March 1963).

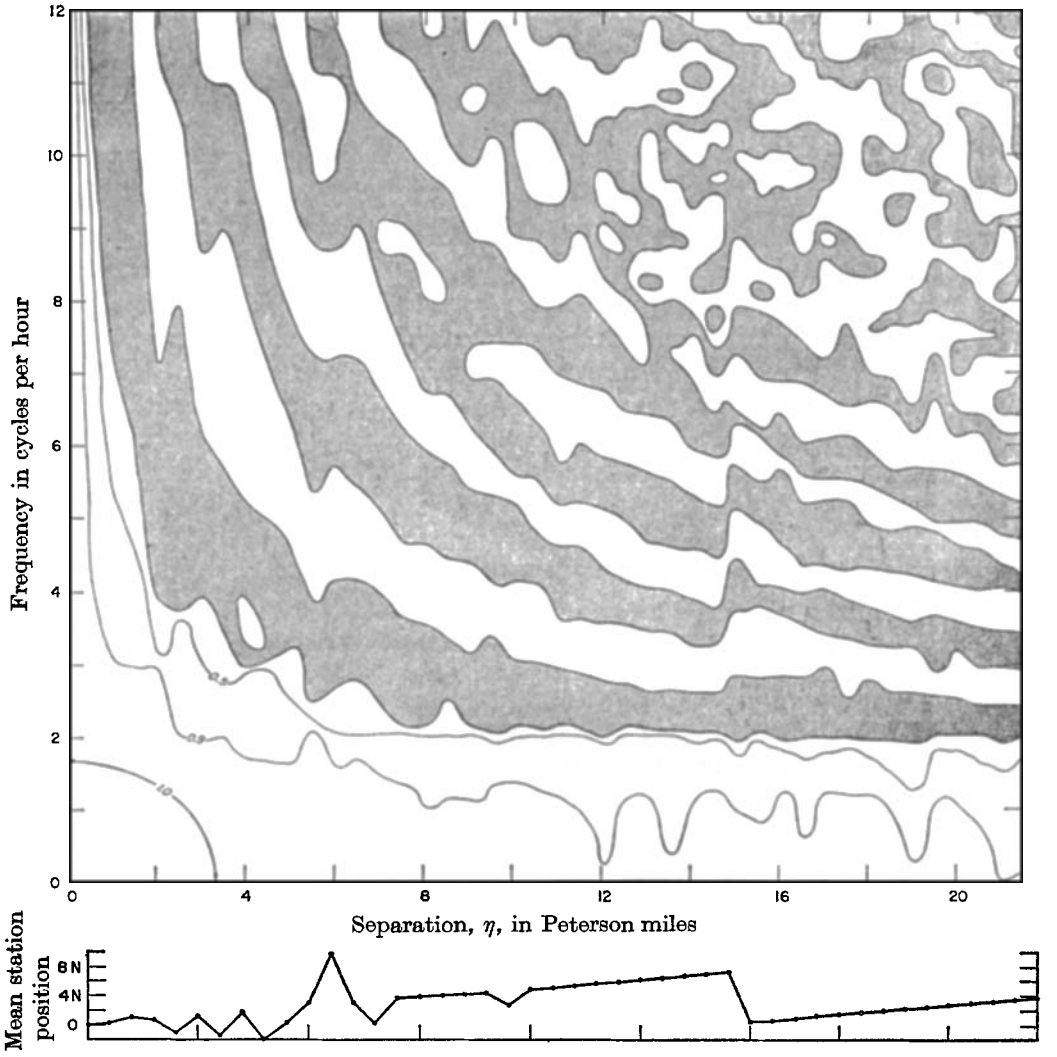

FIGURE 8. The displaced co-spectrum, $C'_N(\eta, f)$. Negative areas are shaded. The bottom display shows the *mean* station position relative to station 0 (figure 1) in Pet. miles.

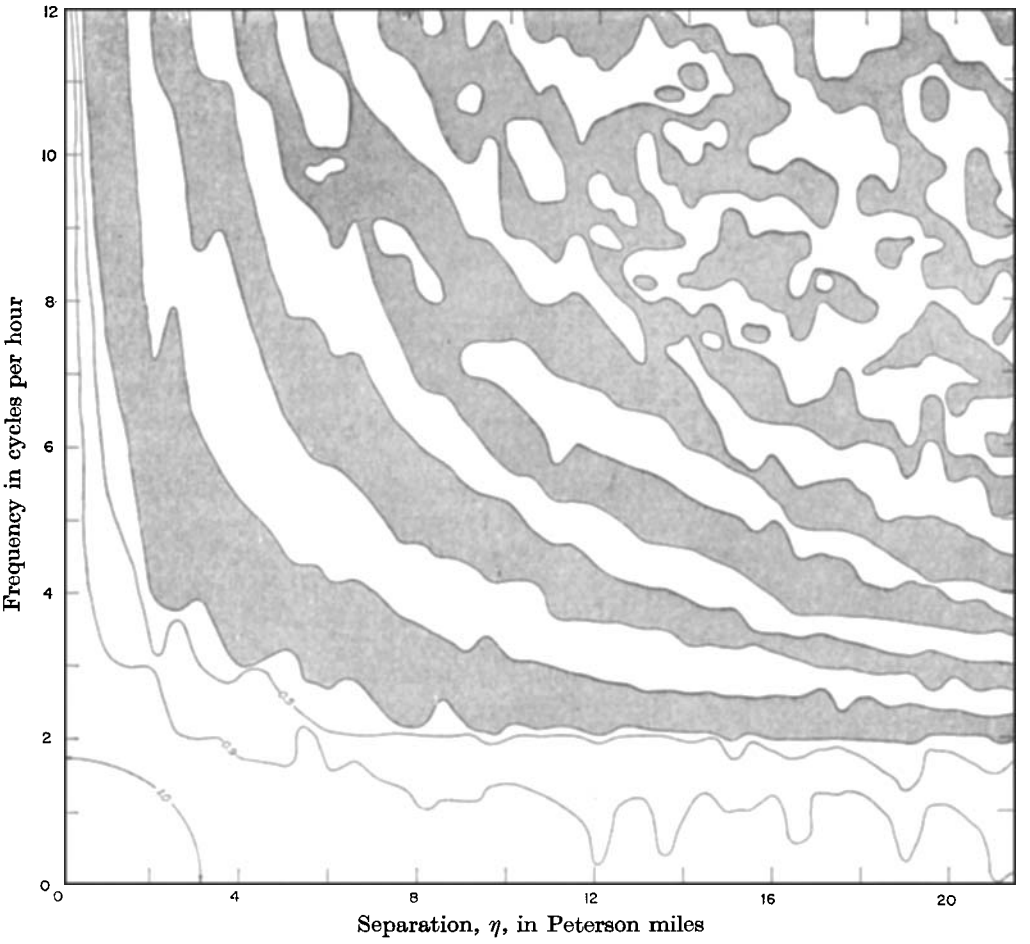

FIGURE 9. The displaced co-spectrum $C'_N(\eta, f)$ adjusted for spatial non-stationarity.

give continuity between $14\frac{1}{2}$ and 15 Pet. miles, using quadratic extrapolation† to compute $C'_N(\eta,f^*)$ from $C'_N(\eta,f)$. A similar adjustment was made at $5\frac{1}{2}$ Pet. miles. The adjusted contours are shown in figure 9. From now on all calculations refer to the fields so adjusted for spatial non-stationarity. One is, of course, always concerned to what extent such an adjustment has imposed conditions on the solution. Figures 10 and 11 show the cosine transforms of the adjusted and non-adjusted fields of $C'_N(\eta,f)$, and there are no essential differences.

† A better procedure would be to compute theoretical (f, n) diagrams for various distances, y, along the coast, and for each of these profiles to obtain the phase velocity, $V(y, f)$, of the appropriate mode. We then replace the station co-ordinate, y, by

$$y^*(f) = V(f, 0)\int_0^y dy/V(f, y)$$

and compute adjusted separations $\eta^*(f)$. But the corrections are small, and the effort to follow this procedure is not worth while.

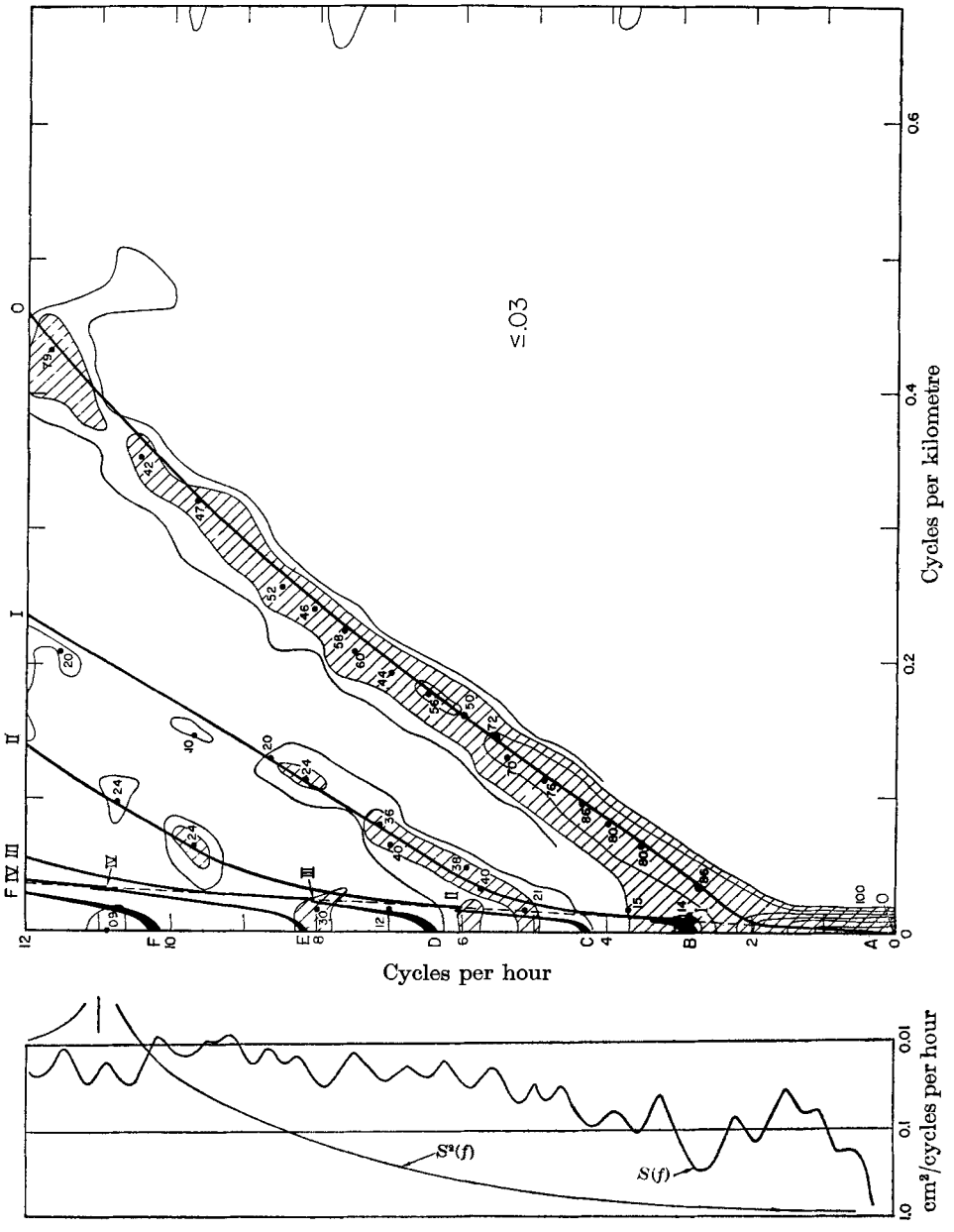

FIGURE 10. Comparison of theoretical and observed dispersion. The heavy lines 0–0, I–I, ..., IV–IV show the theoretical dispersions $f(n)$ for the first five trapped modes. The dashed line through the cut-off frequencies separates the trapped modes to the right from the leaky modes to the left. Solid bands to the left marked A to F show the regions of coastal to deep sea amplification, $r > 1$. The observed power spectrum, $S(f)$, is plotted to the left; $\rho^2(f)$ is the ratio of energy at the instrument to energy at the coast line, for normal incidence. The observed two-dimensional co-spectrum $\frac{1}{2}T^+(n, f)$ is contoured for values of 0·03, 0·05, 0·10, 0·25, 0·50, 0·75, 0·90, with the area above 0·05 units shaded. The units designate the fractional contribution towards $S(f)$ per spatial frequency band $\delta n = 0{\cdot}0159$ c/km. The dots show the observed positions of the ridge and the percentage energy associated with a particular mode.

6. The (f, η) diagram

The contour $C'_N = 1{\cdot}00$ along the axes of figures 8 and 9 is the observed value to two significant figures. Similarly, Q'_N was found to measure 0·00 along the axes. These are the expected values for zero separation and zero frequency, and the precision with which they are attained is a measure of the fidelity of the observations. For $\eta = 0$ the instruments were located within a few metres of one another; the result for $f = 0$ actually includes the effects of frequencies from 0 to 0·1 c/h and thus shows that for periods above 10 h the array does not differ from a point.

The principal feature of the $C'_N(\eta,f)$ plot is an alternating series of arched ridges and troughs which tend to be parallel to the axes for large values of η and f. The features are well defined. The first trough has minimum values of $-0{\cdot}90$, the first ridge has maximum values of 0·90 (at $\eta = 10\frac{1}{2}$ Pet. miles, $f = 3{\cdot}5$ c/h). This means that two instruments separated by $10\frac{1}{2}$ Pet. miles and recording through identical narrow filters peaked at 3·5 c/h will have nearly identical outputs, the mean-square difference being $1 - C^2 = 0{\cdot}19$ times the variance of either record. Four ridges are easily traced, the last reaching peak values of 0·61. In contrast, $Q'_N(\eta,f)$ is so irregular that no sensible contours could be drawn.

For Stokes edge waves over a beach of constant inclination β

$$C'_N(\eta,f) + iQ'_N(\eta,f) = \exp \pm i(4\pi^2\eta f^2/g\beta)$$

with the sign corresponding to the wave direction. Thus if there is equal energy propagated in both directions, then $Q'_N = Q^+_N + Q^-_N = 0$, whereas C'_N has a series of extremi whose axes are given by

$$\eta = \alpha g\beta/(4\pi f^2)$$

with $\alpha = 1, 3, 5, \ldots$ for trough lines, and $\alpha = 2, 4, 6, \ldots$ for ridge lines. This is not unlike the observed pattern. A typical point on the first ridge is $\eta = 9$ km, $f = 5$ c/h, and this leads to a computed inclination

$$\beta = 4\pi^2\eta f^2/2g = 0{\cdot}011$$

as compared to a measured inclination near shore of 0·013. Thus the $C'_N(\eta,f)$ field gives some indication of the prominent role of Stokes edge waves.

7. The (f, n) diagram

Comparison between theory and observations is summarized in figures 10–12. The trapped modes 0–0, I–I, ..., IV–IV, and leaky modes (blackened) A, B, ..., F are marked as in figure 3. The boundary between leaky and trapped modes is now much steeper, and the continuum occupies a small wedge to the left. This is an unfortunate consequence of the limit on spatial frequency resolution imposed by the dimensions of the array. But if we had doubled the array size, we should have experienced even further difficulties with loss of spatial non-stationarity. The ideal place to do the experiment would be a straight coast with a narrow shelf.

The contours give the observed fractional energy distribution; these show a series of narrow bands (or ridges) whose crest (designated by dots) falls embarrassingly close to the computed $f(n)$ relations, lying generally within a few percent.

The interpretation of the numerical values is best illustrated with examples. Table 1 gives the computed values of $\frac{1}{2}T^{+}\delta n$ (the field contoured in figure 10) at 4 c/h for the first nine bands of spatial frequency. Each of these bands has a width of 0·0159 c/km. The first is centred at 0 c/km and extends from − 0·00795 to + 0·00795 c/km; the next is centred at 0·0159 c/km and extends from 0·00795 to 0·02385 c/km, etc. The total fractional energy is found by adding the value at

c/km	0·00	0·0159	0·0318	0·0477	0·0636	0·0795	0·0954	0·1113	0·1273
$\frac{1}{2}T^{+}\delta n$	0·04	0·04	0·04	0·06	0·11	0·14	0·09	0·00	−0·02
Σ for mode 0						0·40			
$\frac{1}{2}T^{-}\delta n$	0·00	−0·01	−0·02	−0·03	−0·04	−0·05	−0·04	−0·02	−0·00
Σ for mode 0						−0·18			

TABLE 1. Fractional energy at 4 c/h per unit spatial frequency band (δn = 0·0159 c/km)

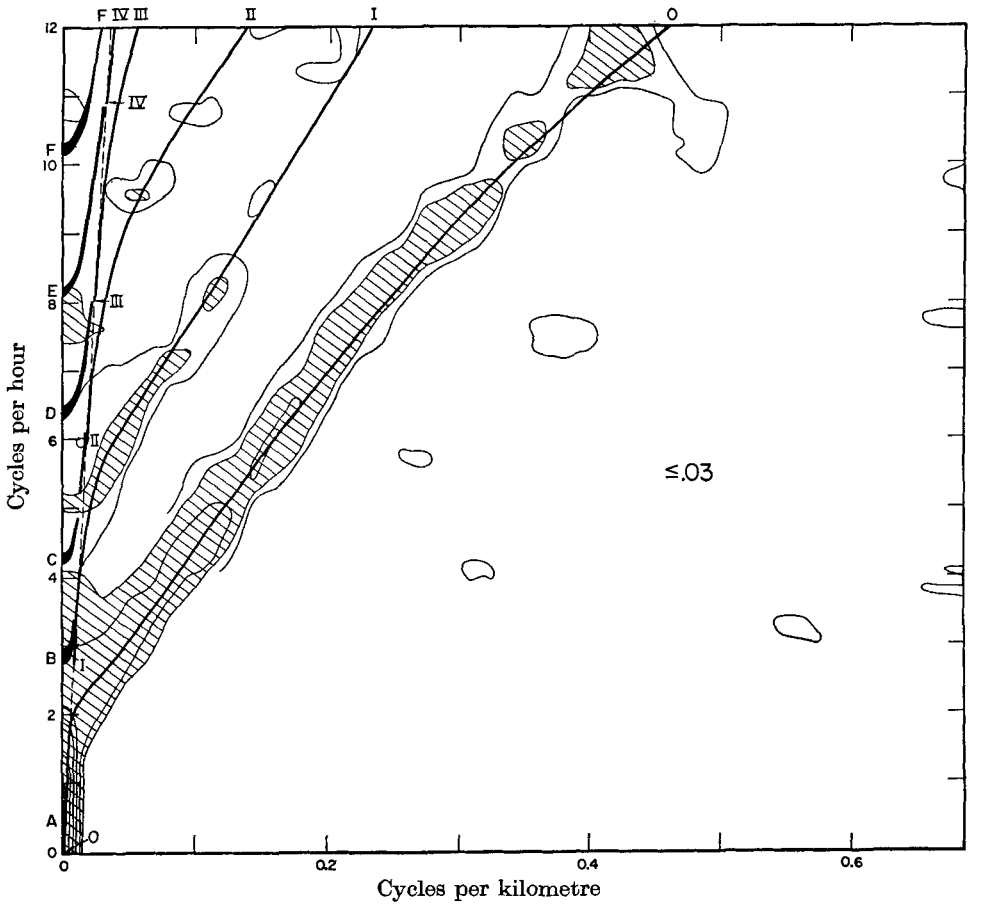

FIGURE 11. The co-spectrum $\frac{1}{2}T^{+}(n, f)$ not adjusted for spatial non-stationarity. For legend, see figure 10.

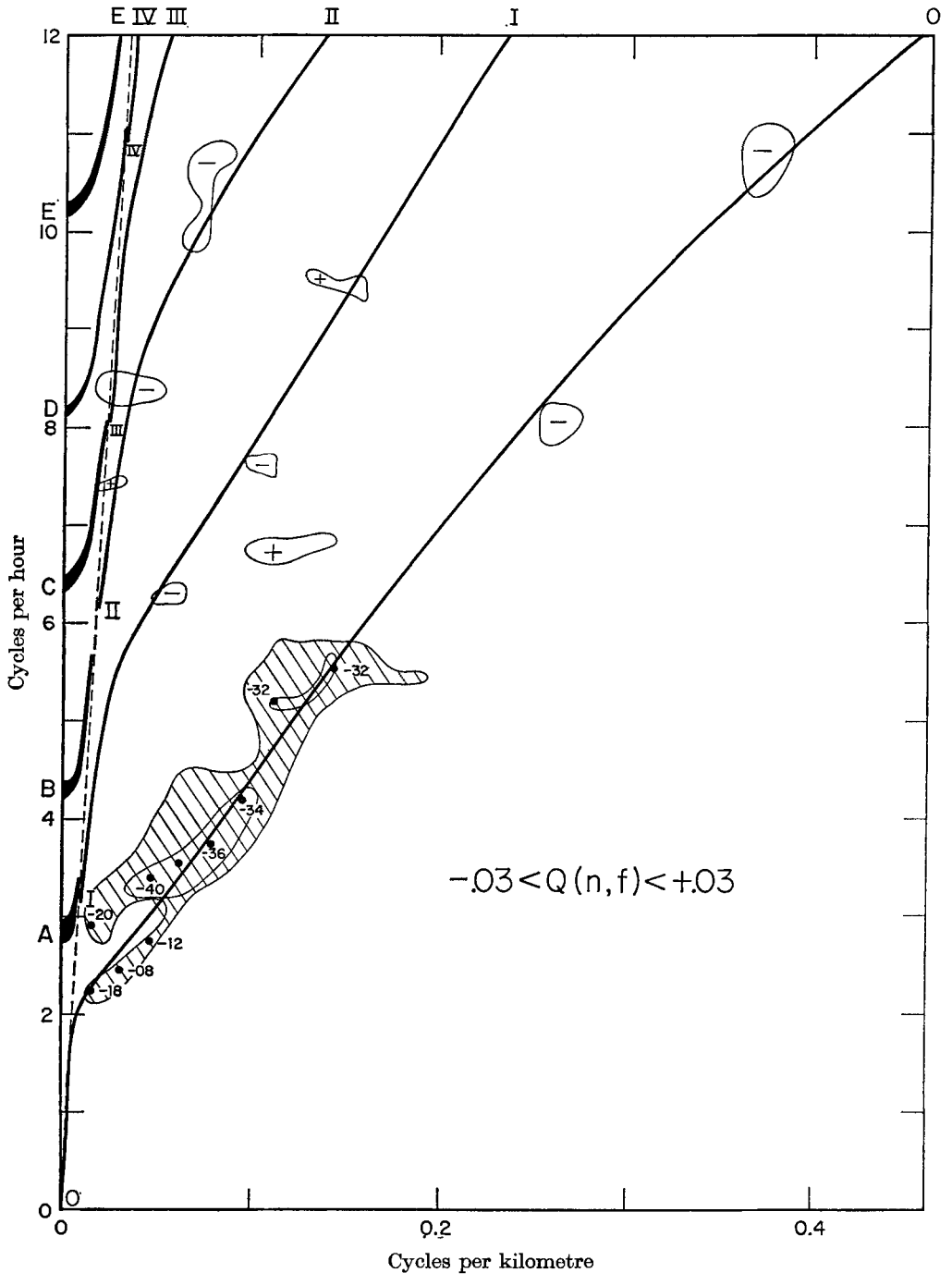

FIGURE 12. The quadrature spectrum $\frac{1}{2}T^{-}(n, f)$ is contoured for values of $-0{\cdot}05$, $-0{\cdot}03$, and $0{\cdot}03$. The shaded areas contain values between $-0{\cdot}05$ and $-0{\cdot}07$. For legend, see figure 10.

0 c/km to *twice* the values in all other bands (up to the spatial Nyquist frequency), thus allowing for positive and negative n:

$$0{\cdot}04 + 2(0{\cdot}04 + 0{\cdot}04 + 0{\cdot}06 + 0{\cdot}11 + 0{\cdot}14 + 0{\cdot}09 + 0{\cdot}00 - 0{\cdot}02 + \ldots).$$

The sum is 0·98, differing slightly from unity owing to round-off error. The contribution from mode 0 (estimated to extend across bands 3 to 8) is twice 0·40, or 80 %, including northward and southward travelling waves. At 4 c/h the energy density is $S(f) = 0{\cdot}1$ cm^2 (c/h)$^{-1}$ (figure 10, left inset), and the total energy in mode 0 is then 0·08 cm^2 (c/h)$^{-1}$.

Next, consider the situation at 7 c/h. The power spectrum (left margin) shows a typical spectral density of 0·025 cm^2 (c/h)$^{-1}$. We find that 44 % of this amount, or 0·011 cm^2 (c/h)$^{-1}$, is contributed by the fundamental mode 0–0, 40 % by mode I, and 12 % by mode II or the continuum. This adds up to 96 %. Energy in the forbidden area between the trapped modes is very low, as it should be. At this frequency of 7 c/h the separation between normal incidence and mode II is only 0·0159 c/km. Twice the maximum array length equals $2 \times 21\frac{1}{2}$ Pet. miles = 62·5 km and the inverse of this is 0·0159 km^{-1}. Thus the estimates at 0 and 0·0159 c/km are not statistically independent.† Lack of spatial frequency resolution is particularly bothersome in trying to assess the relative contributions from the cut-off points of the normal modes, and the f-intercepts of the amplification bands. For example, the observed peak near $f = 8$ c/h, $n = 0$ to 0·0159 c/km is associated either with amplification band E or the cut-off point of normal mode III.

Comparison of theory and observations leads to the following conclusions: (i) most of the energy is in trapped mode 0, though at frequencies of less than 2 c/h it is impossible to distinguish between this mode and leaky mode A; (ii) trapped mode I contributes a maximum of 40 % near 7 c/h, and perhaps half this fraction at high frequencies and near cut-off; (iii) the contribution of trapped mode II is of the same order; (iv) the contribution from leaky modes is generally less than 10 %; (v) the maximum of $S(f)$ at 2·8 c/h corresponds in frequency either to the intercept $n = 0$ of leaky mode B, or to the cut-off frequency of trapped mode 0; (vi) the curve $\rho^2(f)$ on the left margin gives the power reduction at the instrument sites (500 m offshore) relative to the coast line ($x = 0$).‡ A nodal line crosses the instrument site at 11 c/h for normal incidence, and the same result nearly applies to *all* modes except trapped mode 0 (which has no nodal line). The broad minimum in $S(f)$ and the relative lack of contribution from

† In performing the Fourier transforms of $C'_N(\eta, f)$ one meets the customary problems associated with the abrupt termination for separations exceeding η_0. Following the procedure usually adopted in times series analyses (Blackman & Tukey 1958), we multiply $C'_N(\eta, f)$ with 'tapers' which fade out smoothly as η approaches η_0. This reduces side bands from sharp spectral peaks, but at the expense of somewhat widening the central peak. We have used three tapers: (i) TOP-HAT: $H(\eta) = 1$ for $|\eta| \leqslant \eta_0$ and zero elsewhere; (ii) COSINE: $H(\eta) = 1 + \cos \pi\eta/\eta_0$ for $|\eta| \leqslant \eta_0$ and zero elsewhere; and (iii) PARZEN (1961):

$$H(\eta) = 1 - 6(\eta/\eta_0)^2 + 6(\eta/\eta_0)^3$$

for $|\eta| < \frac{1}{2}\eta_0$, $2(1 - \eta/\eta_0)^3$ for $\frac{1}{2}\eta_0 \leqslant |\eta| < \eta_0$, and zero elsewhere. (iii) has no negative side bands and is useful for estimates in the vicinity of a strong peak. The top-hat taper is best for the peak itself, and the cosine taper is a useful compromise. Our discussion is based on the examination of all three transforms.

‡ The ratio of instrument power to incident power is $r^2(f)\rho^2(f)$.

trapped modes I and II between 10 and 12 c/h is then related to distance of the instrument from shore.

Figure 12 shows the fractional difference between southward and northward travelling waves. The field $T^{-}(n,f)$ is largely confined to mode 0, with some slight contributions to modes I and II. At 4 c/h we find for mode 0 (see table 1):

$$\Sigma T^{+}\delta n = \Sigma[S(n,f)+S(-n,f)]\,\delta n/S(f) = 2(0{\cdot}40),$$

$$\Sigma T^{-}\delta n = \Sigma[S(n,f)-S(-n,f)]\,\delta n/S(f) = 2(-0{\cdot}18),$$

so that $$\tfrac{1}{2}[0{\cdot}80 \pm (-0{\cdot}36)] = 0{\cdot}22,\ 0{\cdot}58$$

are the fractional contributions towards $S(f)$ from southward and northward travelling waves, respectively. At higher frequencies and for other modes the contributions from oppositely travelling waves are nearly the same.

8. The situation at higher frequencies

We have also computed (but not displayed) the (f,n) diagrams for frequencies from 0 to 60 c/h at intervals of 0·5 c/h; this is five times the f-scale in figures 10 to 12; the n-scale is unchanged. Again, the gravest trapped modes can be traced, but not as precisely as previously because of the reduction in f-resolution by a factor of five. Modes 0 to V can be recognized. Mode 0 goes off the n-scale ($n > 0{\cdot}7$ c/km) at $f = 14$ c/h; at higher f-values the mode is then associated with n-values above the spatial Nyquist limit, and its energy is folded back into the range 0–0·7 c/km. Similarly, modes I, II, III, IV, V, ... go off the n-scale at $f = 24, 28, 32, 35, 38, \ldots$ c/h, and all their energy is folded back. Thus the diagram at higher f-values is subject to severe spatial aliasing.

f(c/h)	10	15	20	25	30	35	40	45	50	55	60
Relative energy density	0·5	1·9	1·4	0·8	0·6	0·9	2·1	1·0	1·1	1·4	

TABLE 2. Relative energy density in the continuum within stated 5 c/km bands. A relative energy of 1 signifies that the fractional energy in the continuum corresponds to an even distribution over all n-values, from 0 to 0·7 c/km

The purpose of the computations at higher frequencies is to assess the relative contributions from trapped and leaky modes. In table 2 the individual (trapped and leaky) modes are deliberately smudged into 5 c/h bands. At frequencies below 10 c/h the continuum cannot be separated from the cut-offs of the normally incident modes, but there is every indication that the latter contain most of the energy. In the band 10–15 c/h the continuum occupies only the narrow wedge from $n = 0$ to $n = 0{\cdot}03$ c/km out of the total range 0–0·7 c/km, and in this narrow wedge the energy *density* is 0·5 times the mean value, so that the continuum *energy* is $0{\cdot}5(0{\cdot}03/0{\cdot}7) = 0{\cdot}02$. Accordingly, 98 % of the energy is in the discrete modes. At higher frequencies the continuum density fluctuates between $\frac{1}{2}$ and 2 times the mean density, but the continuum energy remains relatively small as compared to the discrete energy.

9. The situation at lower frequencies

A further complication is introduced when the depth profile beyond the continental borderland is taken into account (figures 1 and 2). So far the (f, n) diagrams were computed with the assumption that the borderland extends

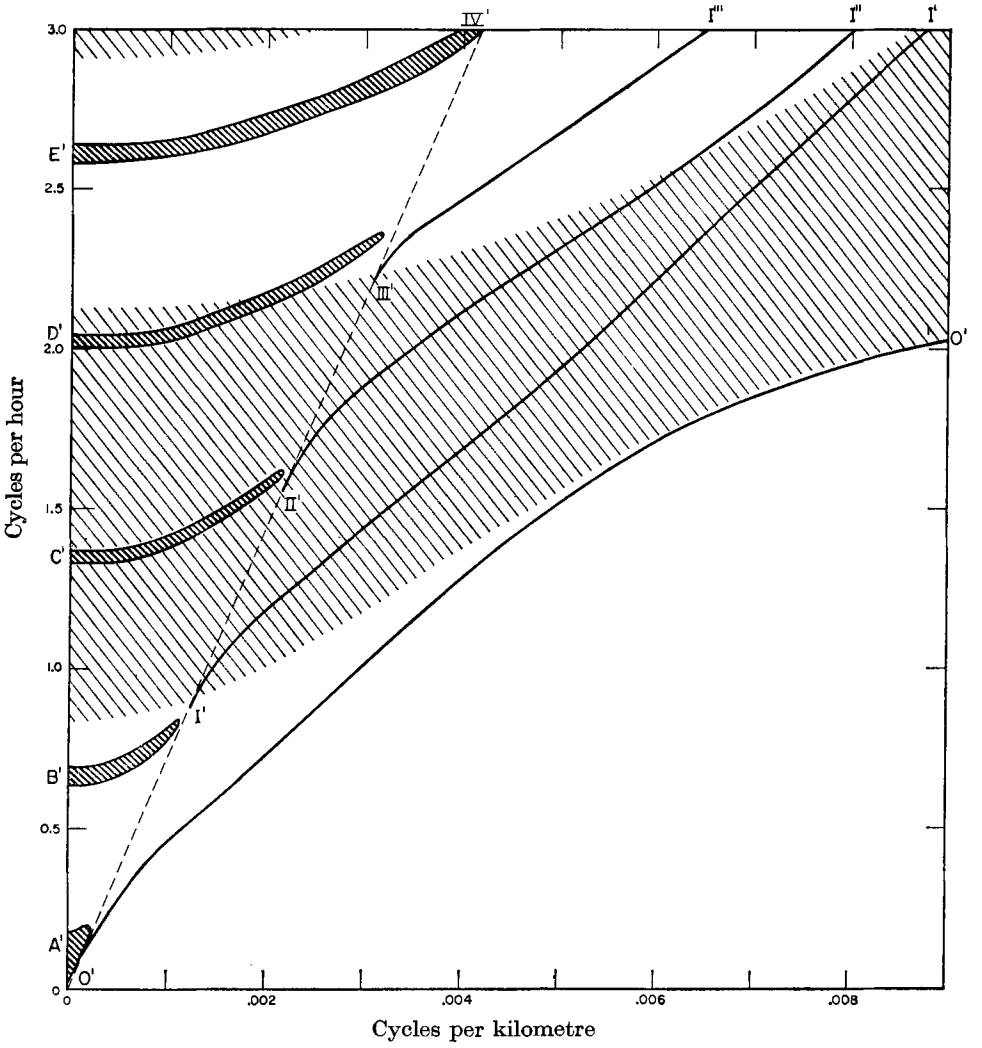

FIGURE 13. The computed (f, n) diagram for a–b continuation, showing trapped modes 0, I′, II , ..., and leaky modes A, B′, C′, ... (see legend figure 3). The shaded bands refer to such combinations of f and n for which waves at $x = 0$ and $x = 100$ km are out-of-phase.

indefinitely in the seaward direction. Inasmuch as the wave energy is essentially confined to a coastal strip whose width is of the order of the longshore wavelength, the present approximation is adequate for waves shorter than the width of the borderland, i.e. $n^{-1} < 200$ km. Longer waves reach seaward beyond the shallow (1 km) borderland into the deep (4 km) Pacific basin, and these are associated with a new set of trapped and leaky modes that are tuned to the dimensions of

the entire borderland. The required modification in going from figure 3 (for profile a–b) to figure 13 (for a–b continuation) can be visualized as follows. The dashed line separating trapped and leaky modes is rotated counterclockwise so as to further confine the area occupied by the continuum. The 'new' trapped mode 0′ is only slightly altered as compared to the 'old' 0. New modes I′, II′, ... have relatively closely spaced cut-off frequencies along the 'new' cut-off line. Mode I′ crosses the old cut-off line near cut-off I and merges with I for large f and n. Mode II′ runs alongside I′ to near cut-off I, then follows the old cut-off line to cut-off II, and merges with II for large f and n. Similarly III′ merges with III, etc. In the a–b continuation a band of mode lines runs along the old a–b cut-off line. In the f or n plane that part of the a–b branch line between its branch point and the a–b continuation branch point is replaced by a chain of roots of equation (9). As f and n decrease, each root successively passes through the new branch point and becomes a new leaky mode in the shrunken continuum. These are the resonances in the open organ pipe sense of the borderland; the harmonic E′ approaches the first shelf resonance B, and the combined borderland and shelf resonances will make this particular leaky mode more prominent than others. To summarize, there is a borderland 'fine structure' at the low frequencies, but the situation is essentially unchanged at high frequencies.

The shaded regions in figure 13 refer to those areas in (f, n) space for which an instrument at the coast would be out-of-phase with an instrument at San Clemente Island 100 km seaward (computed using Haskell matrices, §2). We had previously made simultaneous readings at two such stations (Snodgrass *et al.* 1962) and found sudden phase reversals, with records being in phase for 0–0·72 c/h, out-of-phase between 0·72 and 1·6 c/h, and in phase again above 1·6 c/h. The observed out-of-phase limits 0·7–1·6 c/h are comparable in magnitude to the computed limits, 0·85–2·15 c/h at normal incidence, 0·90–2·25 c/h at glancing incidence, but the situation is too complex to assign the reversals to any particular modes. The assumption of straight parallel contours is no longer tenable at these very low frequencies.

10. Bandwidth

The interpretation of the *width* of the observed bands in figures 10–12 could be interesting. Small-scale wiggles in the coast line and bottom contours must cause scattering from one trapped mode to another, and scattering from the trapped mode into the continuum and vice versa. Such effects would broaden the theoretical line $f(n)$ into a band, and the observed broadening could in turn be interpreted in terms of the coastal scattering cross-section. Scattering interactions, even if they are weak, must play an essential role in determining the distribution of the energy among the various modes.

But before we can interpret the measured broadening along such lines we must be sure it does not arise from more mundane circumstances. In the first place the depth contours vary along the coast. In figure 3 we have plotted the theoretical $f(n)$ relations for two rather extreme profiles; the separation of lines a–b from lines c–d is small compared to the measured bandwidth and this does not appear to be an important source of line broadening.

Next we consider the broadening associated with the limited resolution (time and space). In the case of a one-dimensional process, $x(t)$, the results are familiar. The autocorrelation of $x(t)$ is multiplied by some appropriate fading function, and the Fourier transform is then convoluted with the Fourier transform of the fading function. We have used the Parzen fading function (see §7, first footnote), and its Fourier transform is

$$K(f) = \tfrac{3}{8}(\sin \tfrac{1}{4}\pi F/\tfrac{1}{4}\pi F)^4,$$

where $F = f/\delta f$ is a dimensionless frequency, in units of bandwidth δf. Now if the spectrum is a delta function, then the computed spectrum is $K(F-\hat{F})$, and its mean-square width is

$$\int_{-\infty}^{\infty} F^2 K(F-\hat{F})\,dF = \frac{3}{4}\left(\frac{4}{\pi}\right)^3 \int_0^{\infty} \frac{\sin^4 x}{x^2}\,dx = \frac{12}{\pi^2}.$$

The R.M.S. bandwith in units of frequency $\delta f = 0{\cdot}1$ c/h is $(12/\pi^2)^{\frac{1}{2}}\,\delta f = 0{\cdot}11$c/h. For spatial frequency, $\delta n = 1/2L = 0{\cdot}0159$ c/km, and the theoretical R.M.S. bandwidth is

$$(12/\pi^2)^{\frac{1}{2}}/2L = 0{\cdot}018 \text{ c/km}. \tag{22}$$

Assume all the energy to be concentrated along a line $f(n)$. Because of the limited f-resolution the line is spread over 0·11 c/h along the f-axis, and similarly over 0·018 c/km along the n-axis. For lines of the observed slope df/dn it turns out that essentially all the widening is due to limited n-resolution, and the width of the band along the f-axis is simply the component 0·018 c/km . $\delta f/\delta n$. Poor spatial resolution (a short array) cannot be overcome by good temporal resolution (a long record). The observed R.M.S. width parallel to the n-axis (using the observed values $T^+(n,f)$ for mode 0) is 0·02 c/km, as compared to 0·018 c/km because of limited n-resolution. There is then no evidence for broadening over and above that due to limited spatial resolution.

11. Coriolis splitting

We have discussed the splitting of modes by the continental borderland (§9). An additional source of splitting is the rotation of the Earth. Reid (1958) has shown that if $f_0(n)$ designates the frequency of mode 0 at some fixed n in the absence of rotation, then

$$f_0 + \tfrac{1}{2}\delta f, \quad f_0 - \tfrac{1}{2}\delta f \quad (\delta f = 2\sin\phi/T)$$

are the frequencies of southward and northward travelling waves at latitude ϕ along the west coast of a continent (as in our experiment), with T designating the length of day. Note that δf reverses sign across the equator; in general, the frequency for a fixed n of waves moving to the left (looking seaward) exceeds those moving to the right in the northern hemisphere. The experiment was conducted at latitude 33°, so that $\delta f = 1/T = 1/24$ c/h approximately, about half the resolution attained in the experiment. The detection of any Coriolis effect must be marginal, at best.

Normal modes were found to occupy narrow bands in (f, n) space. The fractional spectra of south- and northward travelling waves at some fixed n can be written

$$-\tfrac{1}{2}\pi^{-\frac{1}{2}}\Sigma(T^+\delta n \pm T^-\delta n)\,k \exp\{-k^2[f-(f_0 \pm \tfrac{1}{2}\delta f)]^2\}.$$

The difference, southward minus northward, gives $T^-(n,f)$ and can be compared to cuts parallel to the f-axis across the observed $T^-(n,f)$ band. The Coriolis shift is small compared to the central frequency and small compared to the bandwidth, or

$$\delta f \ll f_0, \quad k\delta f \ll 1,$$

and so the difference south- minus northward reduces to

$$T^-(n,f) = \pi^{-\frac{1}{2}} k \exp\{-k^2(f-f_0)^2\}[\Sigma T^- \delta n + \Sigma T^+ \delta n k^2 \delta f (f-f_0)].$$

The Coriolis effect is to shift the central frequency of the band from f_0 to

$$f_0 + \tfrac{1}{2}\delta f(\Sigma T^+ \delta n)/(\Sigma T^- \delta n)$$

and to introduce a skewness

$$2^{-\frac{1}{2}}[k\delta f(\Sigma T^+ \delta n)/(\Sigma T^- \delta n)]^3.$$

in the distribution about the band centre. A typical value for $(\Sigma_1' T^+ \delta n)/(\Sigma_1' T^- \delta n)$ is -5, and the resulting shift is by $-0{\cdot}1$ c/h, too low to be measured. The computed skewness varies from $-0{\cdot}003$ to $-0{\cdot}4$. Observed skewness in the T^- field is badly scattered; a representative value is $0{\cdot}5$. The conclusion is that we have failed to observe the Coriolis effect on edge waves because of the limited n-resolution.

12. Summary

We have measured the relative contributions, $S(n,f)$, towards the variance in the oscillation of sea level. Nearly all of the contribution comes from a few well-defined bands. The results can be summarized in terms of the moments

$$\kappa_r = \int n^r S(n,f)\, dn$$

of the bands. κ_0 gives the total band contributions. The trapped mode 0 contains most of the energy, but modes I, II, III contribute significantly. Comparisons of moments for positive and negative n values show that comparable energies are propagated up and down the coast. The contribution from the leaky modes is small.

The moment κ_1 permits a comparison of computed and observed dispersion relations, $f(n)$. The agreement is good. The second moment (properly normalized) is a measure of bandwidth, and this is determined by the spatial resolution in the experiment. The third moment measures skewness. One source of skewness is 'Coriolis-splitting', but this effect is too small to be detectable.

It is surprising that so little of the energy can be associated with waves incident from the open sea, and so much with the waves trapped in the continental wave guide. This may simply be due to the fact that energy is spread fairly evenly along the entire permissible n-axis and so little n-space is available to the continuum. The continuum extends from $n = 0$ to $n = f/(gH)^{\frac{1}{2}}$, H being the (constant) depth beyond the wave guide. The discrete spectra extends from there to $n = 2\pi f^2/g\beta$, where β is the (constant) inclination near shore (this formula for fundamental Stokes edge waves follows from equation (1)). The ratio of continuum n-space to discrete n-space at some frequency f is then

$$\frac{f/(gH)^{\frac{1}{2}}}{(2\pi f^2/g\beta) - f/(gH)^{\frac{1}{2}}} \approx \frac{\beta}{2\pi f}\left(\frac{g}{H}\right)^{\frac{1}{2}}.$$

Setting $f = 10$ c/h, $\beta = 0{\cdot}02$, $H = 1$ km gives a ratio 0·11; for $H = 4$ km it is 0·055. The ratio can be interpreted geometrically as the length of the incident waves in deep water, $f^{-1}(gH)^{\frac{1}{2}}$, divided by the wave guide 'width' $2\pi H/\beta$.

We are grateful to Klaus Hasselmann and Michael Longuet-Higgins for many suggestions concerning this manuscript.

REFERENCES

BLACKMAN, R. B. & TUKEY, J. W. 1958 *The Measurement of Power Spectra.* New York: Dover.

DONN, W. L. 1959 *J. Geophys. Res.* **64**, 191–8.

DONN, W. L. & EWING, M. 1956 *Science*, **64**, 1238–42.

GREENSPAN, H. P. 1956 *J. Fluid Mech.* **1**, 574–92.

HASSELMANN, K., MUNK, W. & MACDONALD, G. 1963 *Time Series Analysis*, pp. 125–39. New York: Wiley.

HASKELL, N. A. 1953 *Bull. Seism. Soc. Amer.* **43**, 17–34.

HASKELL, N. A. 1960 *J. Geophys. Res.* **65**, 4147–50.

INMAN, D., MUNK, W. & BALAY, M. 1961 *Deep-Sea Res.* **8**, 155–64.

LAMB, H. 1932 *Hydrodynamics.* Cambridge University Press.

MUNK, W., SNODGRASS, F. & CARRIER, G. 1956 *Science*, **123**, 127–32.

MUNK, W. H., SNODGRASS, F. E. & TUCKER, M. J. 1959 *Bull. Scripps Inst. Ocean.* **7**, 283–362.

PARZEN, E. 1961 *Technometrics*, **3**, 167–190.

REID, R. O. 1958 *J. Mar. Res.* **16**, 109–44.

ROSENBAUM, J. H. 1960 *J. Geophys. Res.* **65**, 1577–613.

SNODGRASS, F. E. 1964 *Science* (in the Press).

SNODGRASS, F. E., MUNK, W. H. & TUCKER, M. J. 1958 *Trans. Amer. Geophys. Un.* **39**, 114–20.

SNODGRASS, F. E., MUNK, W. H. & MILLER, G. R. 1962 *J. Mar. Res.* **20**, 3–30.

URSELL, F. 1952 *Proc. Roy. Soc.* A, **214**, 79–97.

VOLTERRA, V. 1887 *Mem. Soc. ital. Sci.* **6**, 1–104.